3558 Biophysical Journal Volume 85 December 2003 3558–3574

Model of Bacterial Band Formation in Aerotaxis

B. C. Mazzag,* I. B. Zhulin,† and A. Mogilner‡
*Department of Mathematics, Humboldt State University, Arcata, California 95521; †School of Biology, Georgia Institute of Technology, Atlanta, Georgia 30332; and ‡Laboratory of Cell and Computational Biology, Center for Genetics and Development and Department of Mathematics, University of California, Davis, California 95616

ABSTRACT Aerotaxis is a particular form of "energy taxis". It is based on a largely elusive signal transduction machinery. In aerotaxis, oxygen dissolved in water plays the role of both attractant (at moderate concentrations) and repellent (at high and low concentrations). Cells swimming from favorable oxygen concentrations into regions with unfavorable concentrations increase the frequency of reversals, turn back into the favorable domain, and become effectively trapped there. At the same time, bacteria consume oxygen, creating an oxygen gradient. This behavior leads to a pattern formation phenomenon: bacteria self-organize into a dense band at a certain distance from the air-water interface. We incorporate experimental observations of the aerotactic bacterium, *Azospirillum brasilense*, into a mathematical model. The model consists of a system of differential equations describing swimming bacterial cells and diffusing oxygen. The cells' frequency of reversals depends on the concentration of oxygen and its time derivative while oxygen is depleted by the bacteria. We suggest a hypothetical model of energy sensing mediated by aerotactic receptors Aer and Tsr. Computer simulations and analysis of the model equations allow comparisons of theoretical and experimental results and provide insight into the mechanisms of bacterial pattern formation and underlying signal transduction machinery. We make testable predictions about position and density of the bacterial band.

INTRODUCTION

Chemotaxis

Bacterial chemotaxis is a striking example of cell motility in the direction of higher attractant concentrations and away from repellents (Bray, 2001). *Escherichia coli*, the most well-studied bacteria, swim smoothly in a neutral environment for ~1 s, then for ~0.1 s go through a period of abrupt changes of direction, called tumbling. The sequence of "runs" and "tumbles" results in a random walk that is biased when an added attractant suppresses the frequency of tumbling. As a result, the straight runs lengthen in the direction of higher attractant concentration, allowing the bacteria to move up the attractant gradient. This chemotactic movement relies on a temporal comparison (Brown and Berg, 1974) that requires a memory.

The memory is based on highly conserved signal transduction pathways widely studied in *E. coli* (Bray, 2001; Bourret and Stock, 2002). Binding of an attractant molecule to one of four transmembrane chemotactic receptors induces a conformational change in the receptor's signaling domain in the cytoplasm. Subsequent fast (~0.1 s) activation in CheA-CheY phospho-relay pathway increases the probability of counterclockwise rotation of the flagellar rotary motors. As a result, left-handed flagella bundle together, and the cell swims smoothly. Then, slow (~1–4 s) methylation (adaptation) of the receptors mediated by CheR and CheB enzymes restores the signaling back to the baseline. The probability of clockwise rotation of the flagellar motors increases, the flagella fly apart, and the cell tumbles. An important feature of chemotaxis is accurate adaptation—return of the tumbling frequency to baseline after transient activation (Barkai and Leibler, 1997). (The adaptation needs not be exact, but must be accurate enough to keep the cells near the middle of the flagellar motor response curve (Mello and Tu, 2003).) This keeps the sensory pathways from saturating, and allows cells to remain sensitive to concentration changes in a wide range of chemical environments.

Aerotaxis

Aerotaxis is an active cell movement along gradients of oxygen. This type of bacterial behavior was first described more than 100 years ago by Engelmann, who demonstrated that bacteria aggregated around air bubbles (Engelmann, 1881). Later, Beijerinck observed that bacteria form a band in a particular position in a spatial oxygen gradient, suggesting that bacteria seek optimal oxygen concentration (Adler, 1988). In the process of band formation, bacteria become trapped in a zone that is proposed to have an optimal oxygen concentration (Jennings and Crosby, 1901): cells reaching the edge of the zone on either side reversed their direction of swimming and returned to the band. After these early studies of aerotaxis, this type of microbial behavior has been identified in many bacterial species and a correlation between the metabolic requirements for oxygen (strictly aerobe, facultative anaerobe, microaerophil, anaerobe, etc.) and a position of the aerotactic band in oxygen gradients was observed (Taylor et al., 1999) in all of them. This reinforces the notion that aerotaxis is advantageous for cell survival because finding optimal concentrations of oxygen is critical to cell metabolism and growth. Aerotaxis has a significant ecological role in vertical stratification of microorganisms and their interactions with other organisms (Taylor et al., 1999).

Submitted April 22, 2003, and accepted for publication August 7, 2003.

Address reprint requests to Alexander Mogilner, 682 Kerr Hall, Davis, CA 95616. Tel.: 530-752-1072; E-mail: mogilner@math.ucdavis.edu.

0006-3495/03/12/3558/17 $2.00

Bacteria can sense stimuli either directly via the stimulus-binding mechanism or indirectly, by responding to some change (usually metabolic) caused by the stimulus. Recent studies have demonstrated that the direct and indirect mechanisms are also used for aerotaxis. For example, a sensory receptor that governs aerotaxis in *Halobacterium salinarum* and *Bacillus subtilis* binds to oxygen directly via its heme-containing sensory domain (Hou et al., 2000), whereas two receptors that govern aerotaxis in *E. coli* do not bind oxygen and respond to changes caused by oxygen reduction from the electron transport system (Bibikov et al., 1997; Rebbapragada et al., 1997). In the latter case, aerotaxis is the part of an overall behavior called ''energy taxis'' (Taylor and Zhulin, 1998; Alexandre and Zhulin, 2001; Taylor et al., 1999), where cells monitor the intracellular process of energy generation by the electron transport system and respond to various physicochemical parameters to optimize energy.

Signal transduction in aerotaxis

More than 20 years ago, a ''protometer'' idea for energy sensing was proposed (in Glagolev, 1980). Since then, significant progress has been made in elucidating molecular details of the signal transduction in aerotaxis, but the precise mechanisms remain elusive. The Aer and Tsr transducers of *E. coli* have been identified as two receptors for energy taxis (including aerotaxis) (Rebbapragada et al., 1997). (There are many similarities among four chemotactic receptors, but there are also some differences. Tar receptor is the most well-studied; in this article we model the Tsr pathway based on what is known about Tar.) Both transducers respond to changes in the electron transport (respiratory) system modulated by oxygen. Aer has a flavin adenine dinucleotide cofactor associated with its sensory domain (the so-called PAS domain (Taylor and Zhulin, 1999)), which is thought to detect the redox status of the electron transport system, as it can be readily reduced and oxidized (Repik et al., 2000; Bibikov et al., 1997). In turn, the redox status is the function of oxygen concentration: if the oxygen concentration is too high, the system is fully oxidized, whereas if the oxygen concentration is too low, the system is fully reduced. For optimal electron transport (and therefore optimal energy generation), the system must be in a dynamic equilibrium, e.g., maintain a certain redox status of its components. This redox status would correspond to some optimal concentration of oxygen. It is not known what parameter is measured by the Tsr transducer, but the current hypothesis is that it is the proton motive force generated by the electron transport system (Rebbapragada et al., 1997; Taylor, 1983).

Either Aer or Tsr alone allows for band formation in a capillary and triggers a response in a temporal gradient assay (Rebbapragada et al., 1997), and cells with mutations of either *aer* or *tsr* genes are still aerotactic. However, when both genes are mutated, cells do not exhibit aerotactic behavior (Repik et al., 2000). Also, in a receptorless strain (all four chemotactic transducers and Aer are knocked out), expressing either Aer or Tsr alone restores the band formation in a capillary (Repik et al., 2000). The signals sent by Aer and Tsr are not competing in wild-type cells, and are likely to be additive (Rebbapragada et al., 1997). CheA, CheW, and CheY proteins are essential for aerotaxis (Rowsell et al., 1995) suggesting that Aer and Tsr signaling domains interact with the CheA-CheW complex and regulate the chemotaxis phospho-relay activation pathway from the receptors to the switch on the flagellar motors.

Tsr is known to be methylated in response to chemical stimuli, such as serine (Li et al., 1997). Tsr-mediated aerotactic response is also methylation-dependent and therefore requires the same adaptation machinery as classical chemotaxis. Indeed, in *cheB* mutant, the aerotactic response is inverted (Dang et al., 1986), probably because Tsr is over-methylated by CheR (Taylor and Johnson, 1998). If *tsr* gene is deleted in the *cheB* mutant, then aerotaxis becomes normal again (Dang et al., 1986). This also indicates that Aer is not methylated by CheR; otherwise it would be over-methylated in the absence of CheB and the response would likely be inverted, which is not the case. Further data for methylation-independence of Aer-mediated adaptation include the following observations: i), In *cheB* mutant, where no methylation can take place, or when the source of methyl groups in the cell is depleted biochemically, aerotaxis is observed, whereas chemotaxis is abolished (Niwano and Taylor, 1982). ii), There is no consensus sequence for methylation in the Aer protein (Rebbapragada et al., 1997). iii), Aer does not have the binding sites for CheR and CheB at the end of a C-terminal flexible tether (I. Zhulin, unpublished observation). Proteins that lack these sites cannot be effectively methylated in the absence of Tsr or Tar receptors and their function is substantially compromised (Feng et al., 1997), whereas Aer is functional in the absence of all other chemotactic receptors. The mechanism of the methylation-independent adaptation is unknown. Note that the time required for adaptation to oxygen is shorter than that for adaptation to many other chemo-effectors (Taylor, 1983).

SPATIAL AND TEMPORAL GRADIENT ASSAYS FOR AEROTAXIS IN *AZOSPIRILLUM BRASILENSE*

Azospirillum brasilense as a modeling organism

Azospirillum brasilense (*A.b.*) is a microaerophilic plant-associated bacterium fixing nitrogen under low oxygen concentrations and exhibiting strong aerotactic behavior (Zhulin and Armitage, 1993). There is a significant amount of quantitative data on spatial and temporal gradient aerotactic assays in *A.b.* (Zhulin et al., 1996), making these bacteria a perfect system to model. *A.b.* is 1–2 μm long and has a single polar flagellum (Zhulin and Armitage, 1993).

Flagellar rotation in a counterclockwise direction causes forward movement of free-swimming cells, whereas change in the direction of rotation to clockwise causes a reversal in swimming direction. This mode of locomotion makes reversal angles close to 180°. Therefore, though *A.b.*, like *E. coli*, moves in three dimensions, its directions of swimming before and after a reversal correlate strongly. To some extent, this justifies mathematical modeling of *A.b.* in one dimension, which greatly simplifies the computations. Note that the molecular details of the *A.b.* aerotaxis pathway are not known, and the 3-D random walk of runs and tumbles of *E. coli* cannot be mapped directly onto the 1-D reversals of *A.b.* We model the swimming behavior of *A.b.* in the section ''Mathematical model of the spatial gradient assay for aerotaxis'' (corresponding results in the first four sections of ''Results''), and then the signal transduction pathways of aerotaxis of *E. coli* in the section ''Model of energy sensing'' (corresponding results in the section ''How the cell senses oxygen gradients''). A combination of these models provides valuable insight, but whether such a combination works in a single organism is an open question.

Temporal gradient assay for aerotaxis

A.b. bacterial suspension was exposed to different oxygen concentrations (Zhulin et al., 1996). The frequency of reversals remained approximately constant at 0.22–0.32/s for most variations in oxygen concentrations. However, the frequency dropped to 0.09/s when cells were ventilated with 0.5% oxygen after being equilibrated to nitrogen (no oxygen). The other noticeable change occurred when cells that had been adapted to 0.5% oxygen were exposed to 5% oxygen. In this case, the reversal frequency jumped to 0.49/s. The response of *A.b.* was symmetric: the frequency of reversals reacted similarly to an oxygen decrease as to an increase. Specifically, when oxygen concentration was changed from 0.5 to 0%, the cells increased their reversal frequency, and after change from 5 to 0.5%, the cells responded positively by prolonged swimming. These findings indicate that cells are attracted to ~0.5% oxygen concentration. Furthermore, the proton motive force reached a maximum in the preferred (a few tenths of a percent) oxygen concentration range (Zhulin et al., 1996). The membrane potential, a major component of the proton motive force, decreased after exposure to 1% and 5% oxygen and increased reversibly after lowering the concentration to the preferred level. In this article, we mostly use the oxygen concentration measured in percentage of oxygen in the air (21% is the average concentration under normal conditions.) The corresponding concentration of oxygen in water measured in μM near a surface is linearly proportional to that in air; 1% oxygen in air corresponds to 10 μM in water.

Spatial gradient assay for aerotaxis

In the spatial assay for aerotaxis, a 50 × 2 × 0.1 mm capillary tube was filled with *A.b.* bacterial suspension. At the air-suspension interface (meniscus) at the open end of the capillary, the oxygen concentration was maintained at various fixed levels. A dense bacterial band formed inside the capillary in a period ranging from 50 s to 3 min (Fig. 1) (Zhulin et al., 1996). (This phenomenon was observed earlier; see Barak et al. (1982). Similar assays for *E. coli* and *Salmonella typhimurium* (Shioi et al., 1988) were also investigated.) The distance between the edge of the aerotactic band and the meniscus was a few hundred microns at 21% of oxygen at the open end. When the oxygen concentration at the meniscus was increased to 100%, the band moved a few hundred microns farther away from the meniscus. If nitrogen replaced oxygen, the band moved closer to the open end and eventually disappeared. If air was introduced again, the band reappeared. Furthermore, at a 1% oxygen concentration at the meniscus, there was still a small finite distance of 100–200 μm between the band and the air-suspension interface. In all these experiments, the band's width was ~200 μm. The aerotactic band moved toward the meniscus as the oxygen concentration in the chamber was reduced, and the front of the band was adjacent to the meniscus when the oxygen concentration was 0.5%. A further decrease in oxygen concentration resulted in a decrease in the size of the band, and the band completely disappeared when the oxygen concentration in the gas phase was lowered to 0.02%.

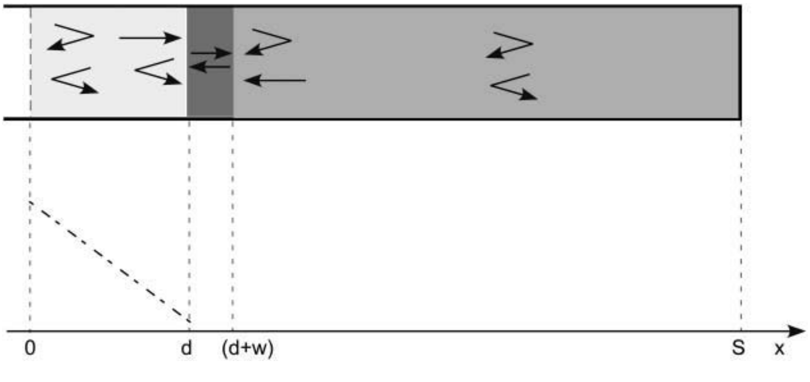

FIGURE 1 Schematic illustration of the spatial assay for *Azospirillum brazilense* aerotaxis (based on Fig. 2 of Zhulin et al. (1996)). The bacterial band of width $w \simeq 0.2$ mm (*dark*) forms at $d \simeq 1.6$ mm from the meniscus (*dashed line* on the *left*). Cells rarely reverse as they swim across the band, or as they swim into the band at its edges (*straight arrows*), whereas they reverse often outside the band, or as they swim away from the band at its edges (*bent arrows*). Bacterial density behind the band (*medium dark*) is significantly lower than that in the band. The density in front of the band (*light*) is orders of magnitude lower than that behind the band. The oxygen concentration (*dash-dotted line*) decreases linearly from the constant level at the meniscus to almost zero at the edge of the band.

The bacterial density inside the band was about an order of magnitude greater than that behind the band, where it remained approximately equal to the density of suspension before pattern formation. The cells were almost completely depleted from the region between the band and the meniscus. The cells swimming in either direction away from the band reversed immediately and returned to the band. The cells swimming into the band from either direction did not reverse until they reached the opposite side of the band. Bacteria in the region in front of the band where the oxygen concentration was above 5% had a random motility pattern (frequency of reversal was ~0.22–0.32/s). Inside the band, the cells swam with an average speed of 49 μm/s, whereas outside the band the average speed was 14–22 μm/s, depending on the oxygen concentration.

After band formation, the profile of oxygen concentration was linear, decreasing from a constant level at the meniscus (21% in the experiment (Zhulin et al., 1996)) to ~0.5% at the front edge of the band (~1.6 mm in the experiment (Zhulin et al., 1996)). The oxygen concentration inside the band seemed to decrease to zero (below sensitivity of the needle oxygen electrode used for the measurements), remaining zero behind the band.

Theoretical approach to aerotaxis

The assays described above indicate that the bacteria are attracted to a specific low concentration of oxygen (3–5 μM correlate to 0.3–0.5%). These values are approximate, since it is hard to determine the effect of bacterial respiration on the oxygen concentration in the band. The gradient of oxygen is established by the cells in the band consuming the oxygen diffusing through the water from the meniscus. Aerotaxis apparently guides the bacteria to a concentration of oxygen that is optimal for energy production. By this hypothesis, bacteria leaving the aerotactic band through the high-oxygen or low-oxygen boundary experience a loss of energy, which increases the reversal frequency resulting in a return to the band. Upon reversal into the band, the energy increase causes the suppression of reversal and leads to the trapping of bacteria within the band.

The following important questions about the aerotactic behavior remain open. They cannot be addressed experimentally due to the limitations of current experimental techniques.

Are quantitative data from the spatial assay consistent with observations from the temporal assay? More specifically, how do the size and density of the band, its distance from the meniscus, and the time necessary for the band formation depend on the oxygen dependent velocities and reversal rates?

How do the width, density, and position of the band relate to the region of favorable oxygen concentrations and oxygen level at the meniscus?

How important is the dependence of the swimming velocity on oxygen concentration?

How are the Aer- and Tsr-mediated signal transduction pathways integrated?

These questions are addressed by computational modeling. Using partial differential equations to describe the movements of bacteria and the diffusion and consumption of oxygen is a suitable technique, because the macroscopic model parameters are known from experiments (Zhulin et al., 1996).

Traditionally, chemotactic movement is modeled with a Keller-Segel drift-diffusion equation (Keller and Segel, 1971):

$$\frac{\partial b}{\partial t} = -\frac{\partial}{\partial x}\left(\left[k\frac{\partial L}{\partial x}\right]b\right) + D_{\mathrm{b}}\frac{\partial^2 b}{\partial x^2},$$

where D_{b} is the effective diffusion coefficient, k is the chemotactic coefficient, and $b(x, t)$ is the space (x) and time (t) dependent cell density. The expression in the square brackets is the simplest possible formula for the rate of the chemotactic drift up the spatial gradient of the chemoattractant, $\partial L/\partial x$. The derivation of this equation is based on the assumption that the chemical gradient is shallow in the sense that it causes very small local differences between the numbers of cell reversals from right to left and from left to right (see a very insightful general discussion of chemotactic equations in Schnitzer et al. (1990)). This condition is not valid in the spatial assay for aerotaxis. Because the bacteria consume oxygen, the oxygen gradients are significant changing over a distance of tenths of microns comparable to the average swimming distance between reversals, and the difference between the numbers of the reversals in two directions near the band's edges is dramatic. In this situation, we use a more basic approach and describe the cells moving in 1-D with two separate equations for the right- and left-moving bacterial densities. Such equations were used for rigorous analysis of bacterial movements (see Othmer and Hillen (2002) and references there).

Quantitative models for aerotactic behavior were considered earlier (Hillesdon et al., 1995; Hillesdon and Pedley, 1996). These addressed aerotaxis in *B. subtilis*, which is attracted to high oxygen concentrations and aggregates to the air-water interface (Wong et al., 1995). The aerotactic behavior of *B. subtilis* is peculiar, because it can be dependent on kinesis, rather than taxis (Wong et al., 1995). The models in (Hillesdon et al., 1995; Hillesdon and Pedley, 1996) used a Keller-Segel-like equation for the bacterial density, which is inappropriate for the aerotactic behavior of *A.b.* They considered complex bio-convection phenomena not relevant to the *A.b.* aerotactic assay. Finally, these models did not rely on the abundant quantitative data about the behavior of *A.b.* Therefore, we suggest here a novel mathematical model (in silico assay) for aerotaxis.

The rest of the article is organized as follows. We describe the models of the spatial aerotactic assay and of the energy-sensing mechanism in the next section. "Results" contains the results of mathematical analysis and computer simulations of the model equations. We discuss the results, implications of the model, and open questions in "Discussion". Mathematical details are gathered in the appendices.

MODEL OF AEROTAXIS

Mathematical model of the spatial gradient assay for aerotaxis

We describe the cells moving in 1-D with equations for the right- and left-moving bacterial densities, $r(x, t)$ and $l(x, t)$, respectively:

$$\frac{\partial r}{\partial t} = -\nu \frac{\partial r}{\partial x} - f_{\mathrm{rl}} r + f_{\mathrm{lr}} l, \quad \frac{\partial l}{\partial t} = \nu \frac{\partial l}{\partial x} + f_{\mathrm{rl}} r - f_{\mathrm{lr}} l. \tag{1}$$

(Right corresponds to the end of the capillary behind the band, whereas left is in front of the band, near the meniscus.) Here ν is the constant swimming speed. In fact, the speed depends locally on the oxygen concentration. However, simulations described below demonstrate that this dependence is insignificant; therefore, we keep the speed constant. f_{rl} and f_{lr} are the frequencies of the reversals from right to left and from left to right, respectively, which depend locally on the oxygen concentration and its derivatives (below). The bacteria do not leave the capillary, so no flux boundary conditions complement the equations of motion. In the case of the simple drift with constant speed, this means that all left-moving cells turn to the right at the left boundary, and similarly, all right-moving cells turn to the left at the right boundary:

$$r(0) = l(0), \quad r(S) = l(S). \tag{2}$$

We also define the bacterial density, $b(x, t) = r(x, t) + l(x, t)$. The conservation of the total number of cells, $\int_0^S b(x,t)\,dt =$ const, follows from Eq. 1. Note that the "telegraph process" described by equations of type Eq. 1 were studied extensively; see Othmer and Schaap (1998) and references there.

In the model, the evolution of oxygen concentration is governed by diffusion across the capillary and the consumption by the bacteria:

$$\frac{\partial L}{\partial t} = D \frac{\partial^2 L}{\partial x^2} - \kappa \theta(L) b. \tag{3}$$

Here $L(x, t)$ is the oxygen concentration, D is the oxygen diffusion coefficient in water, and κ is the rate of consumption. Little is known about the dependence of the rate of consumption on the oxygen concentration; therefore, for simplicity, we assume a constant consumption per cell, independent of the oxygen concentration. The step function $\theta(L) = 1$ at $L > 0$ and $\theta(L) = 0$ at $L \leq 0$ ensures that there is no consumption when oxygen is depleted. The oxygen concentration is constant at the meniscus, and equal to the oxygen level in the air. There is no flux of oxygen at the right end of the capillary:

$$L(0) = L_0, \; \frac{\partial L}{\partial x}(S) = 0. \tag{4}$$

The main assumption of the model is that a cell is able to sense a dynamic change in its internal energy and it is able to change its reversal frequency accordingly. Specifically, we introduce a variable for the internal energy, $E(t)$, that is proportional to the components of the proton motive force and the rate of change in the electron transport (Taylor et al., 1999). Following the observations in (Zhulin et al., 1996), we assume that the cell energy is maximal and constant, E_{max}, in the favorable oxygen interval $L_{\mathrm{min}} < L < L_{\mathrm{max}}$ and that it is minimal and constant, E_{min}, in the unfavorable oxygen regions of low $(L < \tilde{L}_{\mathrm{min}})$ and high $(L > \tilde{L}_{\mathrm{max}})$ oxygen. The energy is an increasing function of the oxygen concentration in the lower sensitive oxygen interval $\tilde{L}_{\mathrm{min}} < L < L_{\mathrm{min}}$ and decreasing in the upper sensitive oxygen interval $L_{\mathrm{max}} < L < \tilde{L}_{\mathrm{max}}$. For simplicity, we approximate the cell energy by the piecewise linear function shown in Fig. 2 *a*.

Following clues from the measurements in Zhulin et al. (1996), we postulate that the reversal frequency is large (small), when the energy is constant and low (high). More importantly, the reversal frequency is large (small) at intermediate and decreasing (increasing) energy. Formally, the reversal frequency, $f(E, dE/dt)$, is given by the following formula (Fig. 2 *b*):

$$f(E, dE/dt) = \begin{cases} F, & E = E_{\mathrm{min}} \\ \frac{1}{2}[(f+F) + (f-F) \cdot sign(dE/dt)], & E_{\mathrm{min}} < E < E_{\mathrm{max}} \\ f, & E = E_{\mathrm{max}} \end{cases}. \tag{5}$$

Note that at intermediate energy, $f(E, dE/dt) = F$ at $dE/dt < 0$, and $f(E, dE/dt) = f$ at $dE/dt > 0$.

A formula giving the reversal frequency as a function of a local concentration field and its material gradient was proposed by Nossal (1976) and Rivero et al. (1989) based on experimental observations of *E. coli* (Berg and Brown, 1972). Such a formula arises from the fact that bacteria sense changes in their surrounding environment by means of a temporal comparison mechanism that has short-term but no long-term memory (Berg and Brown, 1972; Taylor et al., 1999). In our case, the idea that the cell estimates the material gradient of its internal energy, dE/dt, means that the reversal frequency is the function of the rate of change of oxygen in the vicinity of the moving cell. Indeed, the cell effectively measures the derivative $dE/dt = (dE/dL) \cdot (dL/dt)$, where E is the function of oxygen in water around the moving cell. The material gradient of oxygen for the right moving cells is $dL/dt = \partial L/\partial t + \nu \partial L/\partial x$, whereas for the left moving cells, $dL/dt = \partial L/\partial t - \nu \partial L/\partial x$. This leads to the following formulae for the reversal frequencies in Eq. 1:

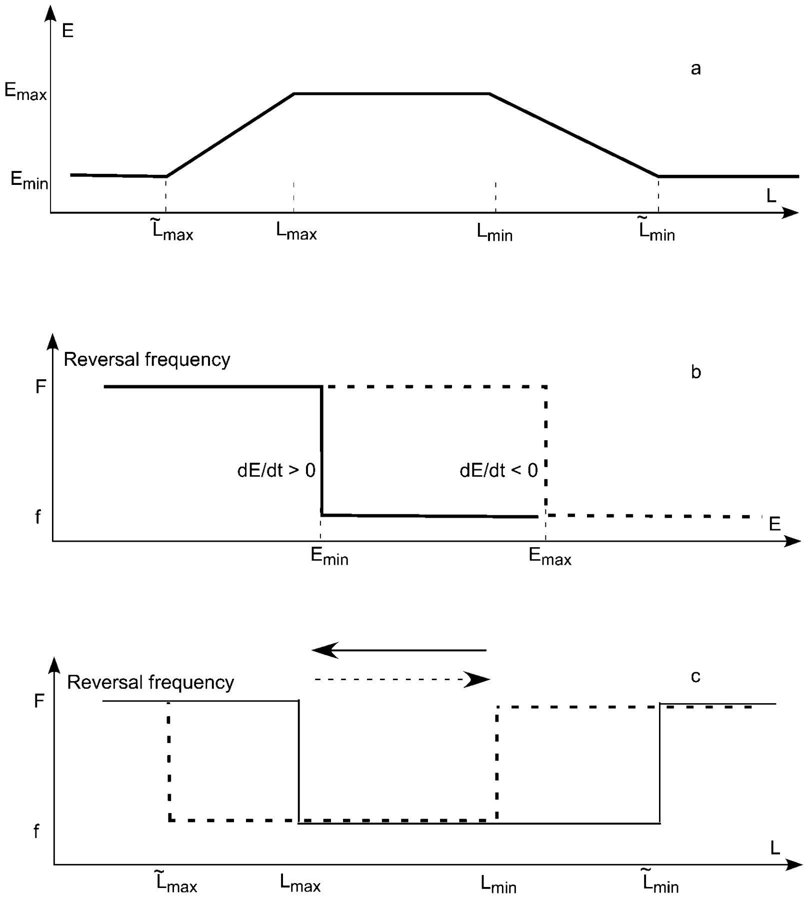

FIGURE 2 (*a*) Internal cell energy, *E*, as the function of the oxygen concentration, *L*, in the model (based on observations of Zhulin et al. (1996)). Note that the oxygen concentration is descending to the right to make this figure consistent with Fig. 1. The reversal frequency versus the energy, *E*, in the model at increasing (*solid line*) and decreasing (*dashed line*) energy. (*c*). The reversal frequency of the right-swimming (*dashed line*) and left-swimming (*solid line*) cells in the stationary oxygen gradient decreasing from left to right.

$$f_{\mathrm{rl}} = f\left(E, \left[\frac{dE}{dL}\cdot\left(\frac{\partial L}{\partial t} + \nu\frac{\partial L}{\partial x}\right)\right]\right),$$
$$f_{\mathrm{lr}} = f\left(E, \left[\frac{dE}{dL}\cdot\left(\frac{\partial L}{\partial t} - \nu\frac{\partial L}{\partial x}\right)\right]\right), \qquad (6)$$

where the function $f(E, dE/dt)$ is defined in Eq. 5, and $dE/dL > 0$ at $\tilde{L}_{\min} < L < L_{\min}$, $dE/dL < 0$ at $L_{\max} < L < \tilde{L}_{\max}$, and $dE/dL = 0$ otherwise.

The model dependence of the reversal frequency on the oxygen concentration displays a hysteresis (Fig. 2 *c*), which is crucial for the model of aerotaxis. When the bacterial band assembles, the steady oxygen concentration in the band is favorable, and cells turn rarely when swimming across the band. To the left of the band, the cells swimming away from the band go up the oxygen gradient into the upper sensitive region. The energy of these cells decreases, their reversal frequency jumps, and they turn back. On the other hand, the cells swimming into the band at the same location experience decreasing oxygen concentration, their reversal frequency drops, and they continue to move into the band. Note that the reversal frequency is determined by the local oxygen concentration and gradient and by the direction of cell swimming only in steady oxygen gradients. During time transients, the reversal frequency also depends on the temporal derivative of oxygen.

Equations 1–6 constitute the mathematical model of the spatial aerotactic assay. Estimates for the model parameters based on the literature are given in Table 1. The values of the parameters and definitions of variables used in the simulations are listed in Table 2.

Model of energy sensing

We complement the phenomenological model of the spatial aerotactic assay for *A.b.* above by a simple hypothetical model of energy sensing (based on the data known for *E. coli*). This model is useful when thinking about the aerotactic signal transduction pathways in semiquantitative terms and for justifying the postulated formula (Eq. 5) for the energy dependence of the reversal frequency. The model is based on the idea that two receptor proteins, Aer and Tsr, sense oxygen concentration instantly by monitoring components of the cell energy level proportional to the oxygen concentration. A change in oxygen induces conformational changes that trigger a fast phospho-relay activation pathway from the receptors to the switch on the flagellar motors.

TABLE 1 Data from spatial and temporal aerotactic assays

Symbol	Range of values	Meaning	Reference
f, F	0.1–0.5/s	Reversal frequency	Zhulin et al. (1996)
ν	20–50 μm/s	Swimming speed	Zhulin et al. (1996)
D	$\simeq 2 \cdot 10^{-9}$ m^2/s	Oxygen diffusion coefficient in water	Hillesdon et al. (1995); Hillesdon and Pedley (1996)
κ	$\sim 10^{-10}$ μmol/(min·cell)	Oxygen consumption rate	Alexandre et al. (1999)
b_0	$\sim 10^8$ cell/ml	Average cell density	Zhulin et al. (1996)
L_0	0–100% (0–1.2 mM)	Oxygen concentration at the air-water interface	Zhulin et al. (1996)
$L_{\max}$	~0.5%	Upper favorable oxygen concentration	Zhulin et al. (1996)
$L_{\min}$	~0.3%	Lower favorable oxygen concentration	Zhulin et al. (1996)
$\tilde{L}_{\max}$	~5%	Upper detectable oxygen concentration	Zhulin et al. (1996)
$\tilde{L}_{\min}$	~0.02%	Lower detectable oxygen concentration	Zhulin et al. (1996)
d	0–2 mm	Distance between the band and the air-water interface	Zhulin et al. (1996)
w	~200 μm	Width of the band	Zhulin et al. (1996)

TABLE 2 Model variables and parameters

Symbol	Dimensional value	Nondimensional value	Meaning
t	~ Minutes	Tens of time units	Time
x	~ Millimeters	Tens of length units	Spatial coordinate
$r(x, t)$	10^8–10^9 cell/ml	1–10	Density of right-swimming bacteria
$l(x, t)$	10^8–10^9 cell/ml	1–10	Density of left-swimming bacteria
$b(x, t)$	10^8–10^9 cell/ml	1–10	Bacterial density
$L(x, t)$	0–100% (0–1.2 mM)	0–1	Oxygen concentration
L_0	0–100% (0–1.2 mM)	1	Oxygen concentration at $x = 0$
$L_{\max}$	0.5%	0.025	Upper favorable oxygen concentration
$L_{\min}$	0.3%	0.015	Lower favorable oxygen concentration
$\tilde{L}_{\max}$	5%	0.25	Upper detectable oxygen concentration
$\tilde{L}_{\min}$	0.01%	0.0005	Lower detectable oxygen concentration
b_0	10^8 cell/ml	1	Initial cell density
κ	10^{-9} (μM·ml)/(s · cell)	10	Oxygen consumption rate
D	$2 \cdot 10^3$ μm^2/s	0.5	Oxygen diffusion coefficient in water
ν	40 μm/s	1	Swimming speed
f	0.1/s	0.25	Low reversal frequency
F	0.5/s	1.25	High reversal frequency
S	4 mm	40	Length of the capillary

Subsequent slow adaptation pathways are responsible for temporal comparison of energy levels.

Fig. 3 illustrates the model. Dynamic equilibrium between inactivated (Aer and Tsr) and activated (Aer* and Tsr*) states of the aerotactic receptors is shifted toward activation by an instant growth of the activation rates in response to the increased cell energy. We assume that activated receptors phosphorylate CheY fast, independently, and additively. We suggest, following (Barkai and Leibler, 1997), that only methylated Tsr receptors are activated (both Tsr and Tsr* in Fig. 3 illustrate methylated proteins). We adopt the reduced model (Barkai and Leibler, 1997), according to which CheR mediates methylation of Tsr receptors in their inactive conformation (in a saturated regime), whereas CheB demethylates only active Tsr receptors. This slow (relative to the fast phosphorylation) methylation/demethylation pathway is responsible for classical CheB/CheR-mediated adaptation of Tsr-induced activation. We propose, following a novel idea of Almogy et al. (2001), that in addition to the methylation-dependent adaptation, one or more methylation-independent pathways exist that are based on CheY$_\text{p}$ dephosphorylation. Two modules of this pathway were suggested in Almogy et al. (2001): one is based on the release of CheA$_\text{s}$ from the active receptors, and another, simpler pathway is based on direct dephosphorylation of CheY$_\text{p}$ by CheZ. Here, for the sake of simplicity, we adopt only the latter: CheY$_\text{p}$ mediates activation of CheZ, whereas activated CheZ mediates dephosphorylation of CheY$_\text{p}$. (An additional reason for this choice is that the chosen module is based on experimental evidence, whereas the other module is hypothetical.) This negative feedback slowly decreases CheY$_\text{p}$ concentration after its fast initial increase after Aer and Tsr activation. Note that the Tsr-driven methylation-dependent pathway alone would be responsible for the exact adaptation (Barkai and Leibler, 1997): CheY$_\text{p}$ concentration would return to the baseline after an initial change. On the other hand, methylation-independent pathway(s) would be triggered by both Aer and Tsr, and would lead to a secondary, imperfect adaptation. We propose that a combination of such primary and secondary pathways, which was shown to increase the accuracy of the cell response (Almogy et al., 2001), takes place in aerotaxis.

Elaborate computational models of chemotactic pathways were proposed previously (Almogy et al., 2001; Barkai and Leibler, 1997; Bray et al., 1993; Segel et al., 1986; Spiro et al., 1997). We do not present the comparison of these models, and we adapt the reduced variants of two of them (Almogy et al., 2001; Barkai and Leibler, 1997) based solely on their mathematical simplicity. (Also, other equally simple and insightful models could be used (see Othmer and Schaap (1998).) We formulate our mathematical model in Appendix 1. In the end of the next section, we report the results of the model simulations that justify formula Eq. 5 and shed light on aerotactic behavior of *aer* and *tsr* mutants.

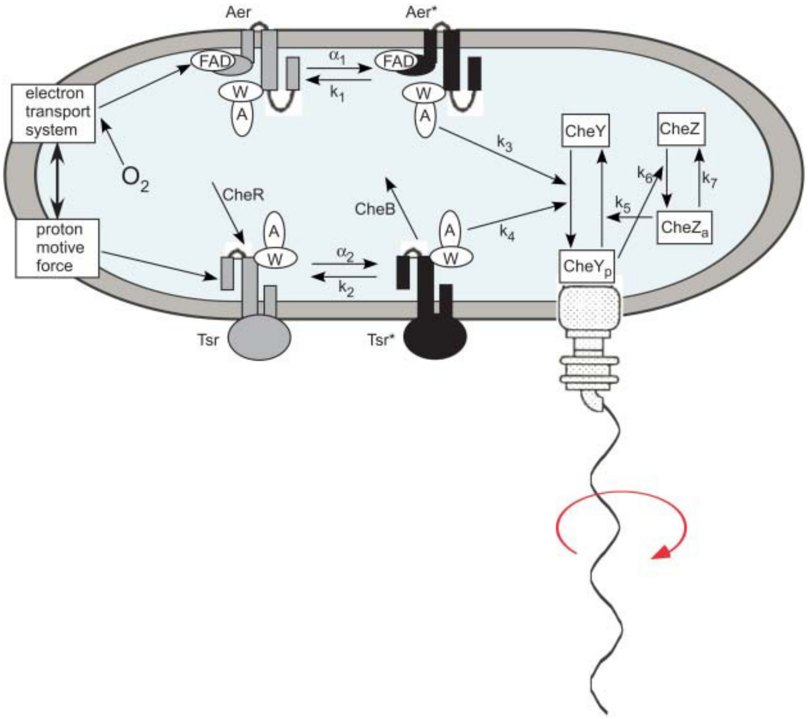

FIGURE 3 Model for energy sensing. Decrease in the proton motive force triggers conformational changes in two aerotactic receptors (Aer, Tsr → Aer*, Tsr*), which induce fast phosphorylation of CheY increasing reversal frequency. Methylation-dependent adaptation pathway associated with Tsr together with methylation-independent adaptation pathway based on dephosphorylation of $CheY_p$ by CheZ are responsible for temporal comparison of the cell energy.

RESULTS

Development of the aerotactic band

We scaled, nondimensionalized, and solved the equations of the spatial assay model numerically as described in Appendix 2. In the simulations, the initial left- and right-moving bacterial densities are equal and homogeneous in the interval. The initial condition for the oxygen concentration is L_0 at the left boundary and zero everywhere else. Results of the simulations are presented in Figs. 4–6.

The development of the aerotactic band at $L_0 = 21\%$ can be gleaned from Fig. 4. In the first few seconds (Fig. 4 *A*), oxygen begins to diffuse into the capillary, and an oxygen gradient evolves. The cells at the open end of the capillary exposed to high oxygen concentrations start swimming toward the lower, optimal oxygen concentrations. Meanwhile, some of the bacteria at the back are also able to detect the lower optimal oxygen level. Therefore, the aggregation into the nascent band begins from both sides, depleting the cells from the sensitive regions near the band edges. The bacterial band continues to move away from high oxygen concentration growing in density by trapping the bacteria in the band's path (Fig. 4 *B*). There is low bacterial density on either side of the band, because all cells at these positions are able to swim into the optimal range.

The band almost reaches its steady-state location, density, and width after 1 min (Fig. 4 *C*). The timescale of the band formation determined by the time for oxygen to diffuse into the capillary, the time for cells to swim away from the high oxygen concentration, and the time for the cells to consume oxygen (all of the same order of magnitude, see Appendix 2) agrees with observations well (Zhulin et al., 1996). The bacterial density in the band, the width of the band, and the distance of the band from the meniscus, analyzed and explained below, are also in semiquantitative agreement with experimental measurements (Figs. 1 and 2 in Zhulin et al. (1996)). Note also that a linear oxygen gradient developed in front of the band, indicating that the constant flux of the oxygen from the meniscus into the band was established. All this flux is consumed by the cells in the band; consumption near the meniscus is negligible because of the very low density of cells there. Note that the sharp peak in the bacterial density in Fig. 4 is an artifact of the numerical scheme; the discretization step in the simulations is 0.1 mm greater than the width of the region where the oxygen concentration is optimal, which is <0.1 mm. Thus, the spatial resolution of the numerical simulations is too coarse to show the plateau in the bacterial density in the region of the optimal oxygen density.

In the next few minutes (Fig. 4 *D*), the densities of bacteria in front of and behind the band equilibrate to constant values due to effective diffusion of the bacteria in these regions. Almost all bacteria from the front have aggregated into the band. Cells behind the band never sense the oxygen, and the bacterial density there remains practically unchanged. The ratio of the cell density inside the band to that in front of the band is >100. Similar ratio of the densities in and behind the band is close to 10. Both of these values agree well with the experimental data. Simulations also demonstrate that after the band has formed, the frequency of actual reversals at the center of the band is very close to zero, whereas at the edges of the band almost all the reversals are back into the band.

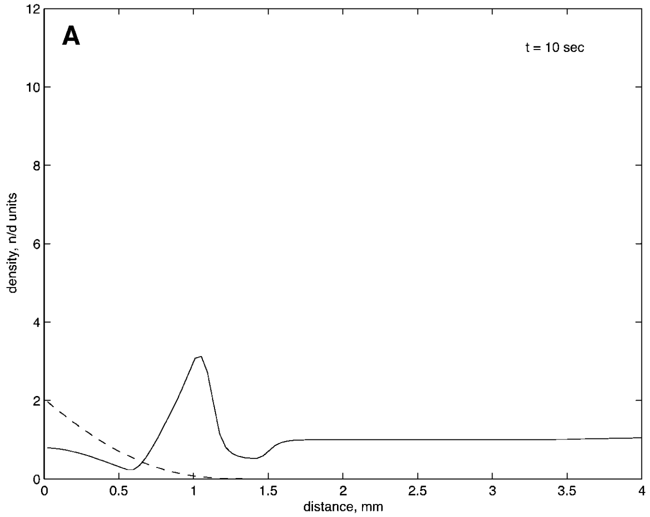

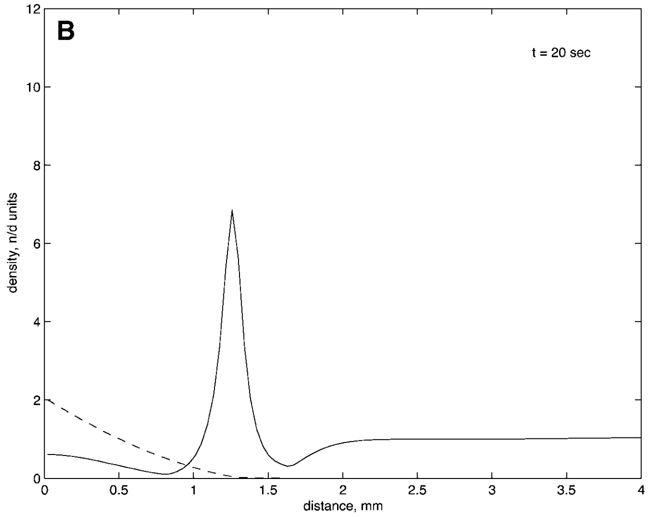

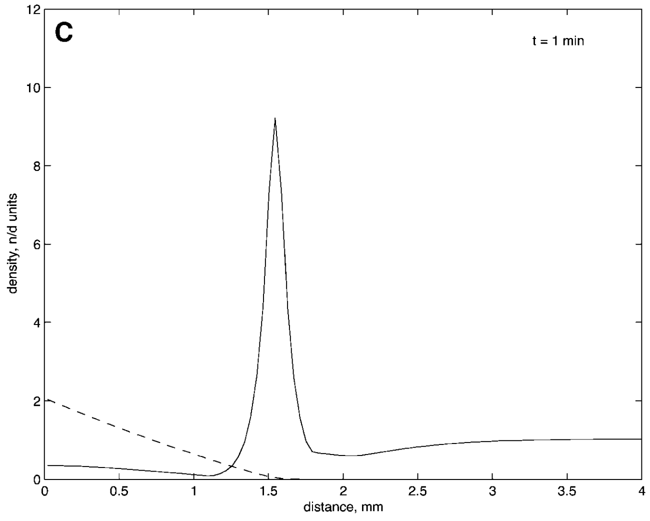

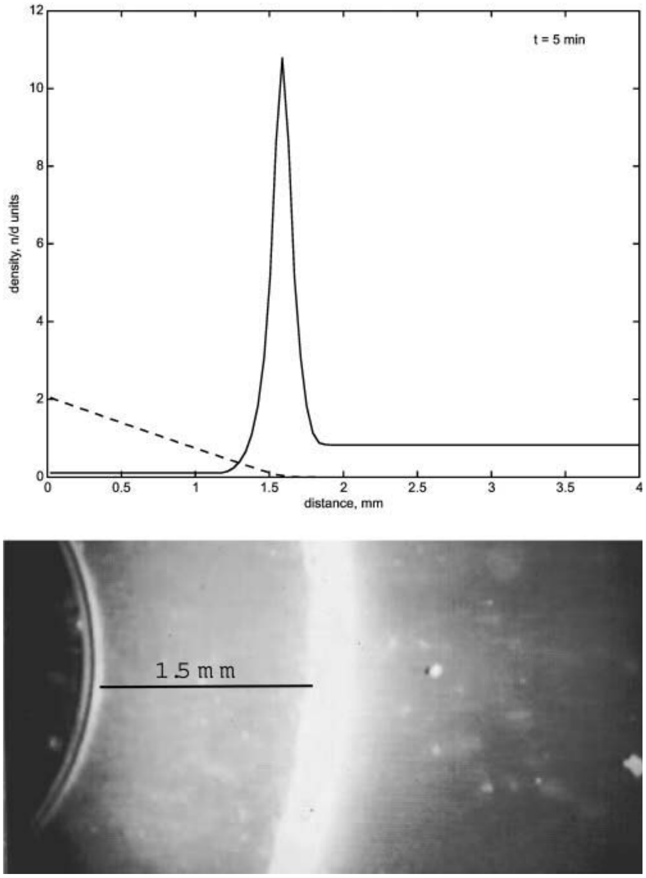

FIGURE 4 Snapshots from the numerical simulations of the model equations at $t = 10$ and 20 s and 1 and 5 min. Bacterial density (*solid line*) and oxygen concentration (*dashed line*) are shown. Initially, the bacterial density is constant, and oxygen concentration is zero everywhere. The following parameters were used: $L_0 = 21\%$, $L_{\max} = 0.5\%$, $L_{\min} = 0.3\%$, $\tilde{L}_{\max} = 5\%$, $\tilde{L}_{\min} = 0.01\%$. In *D*, the bottom plate shows the position of the aerotactic band in the oxygen gradient. The meniscus is the arc at the left. This plate was obtained as described in ''Materials and Methods'' in Zhulin et al. (1996).

The distance between the band and the meniscus and band's density are increasing functions of the oxygen level at the meniscus

By varying the value of the oxygen level at the meniscus, L_0, we demonstrated that the distance between the band and meniscus was an increasing function of L_0 (Fig. 5, *A* and *B*). The reason is clear—the bacteria have to move farther away to escape a higher, harmful oxygen level. This agrees with the experimental observations (Zhulin et al., 1996). The bacterial density in the band also grows when the oxygen level at the meniscus rises (the reason for this effect is discussed below).

When the oxygen level at the meniscus becomes equal to or less than $L_{\max}$, the band forms right at the meniscus (Fig. 5 *C*), clearly because the favorable oxygen concentration then exists at the air-water interface. In agreement with the experiment (Zhulin et al., 1996), the band's density and width were increasing functions of L_0 (Fig. 5 *C*), because a greater oxygen concentration provided a longer time for consumption, allowing more cells from a wider area to swim into the band.

Asymptotic stationary distributions of bacteria and oxygen

Transient solutions of the model equations were found numerically. However, the asymptotically stable stationary distributions of bacteria and oxygen can be obtained analytically because the nonlinear model equations are piecewise linear. In the steady state, the system of differential equations can be solved on intervals and replaced with algebraic equations. This is done in Appendix 3, and the solution provides substantial insight into the relations between the bacterial band's parameters and cell behavior.

The analytical solution demonstrates that the order of magnitude of the band's width is $w \approx 2s = 2\nu/(F-f) = 200$ μm. Furthermore, the distance between the band and meniscus is $d \approx \sqrt{DL_0/\kappa b_0} \approx 1.6$ mm. Finally, the average density of the cells in the band is $\sim(d/2s)b_0 = \sqrt{DL_0 b_0/4\kappa s^2} \approx 8b_0$.

These results are easy to understand with the following estimates. The numerical solution shows that almost all cells in front of the band become trapped in the band, whereas almost all cells behind the band remain there. Because of the conservation of the total number of bacteria, all $B = (b_0 d)$ cells, initially spread homogeneously with density b_0 across the region of depth d (distance between the band and meniscus), are eventually concentrated in the band of width $w \approx 2s$. Therefore, the average density of the cells in the band is $\sim(b_0 d)/2s$. The cells in the band consume κB μM of oxygen per second. This oxygen is delivered by a constant diffusive flux, which is equal to the diffusion coefficient times the oxygen gradient, DL_0/d (the concentration of oxygen drops linearly from L_0 at the meniscus to the very small value in the band over the distance d). The balance of diffusing and consumed oxygen gives the equation $DL_0/d \approx \kappa b_0 d$, from which we can find $d \approx \sqrt{DL_0/\kappa b_0}$.

The analytical estimates for the band's location, density, and width agree well with both numerical results and biological observations. Moreover, they predict that the distance between the band and the meniscus is proportional to the square root of the oxygen level at the meniscus, and

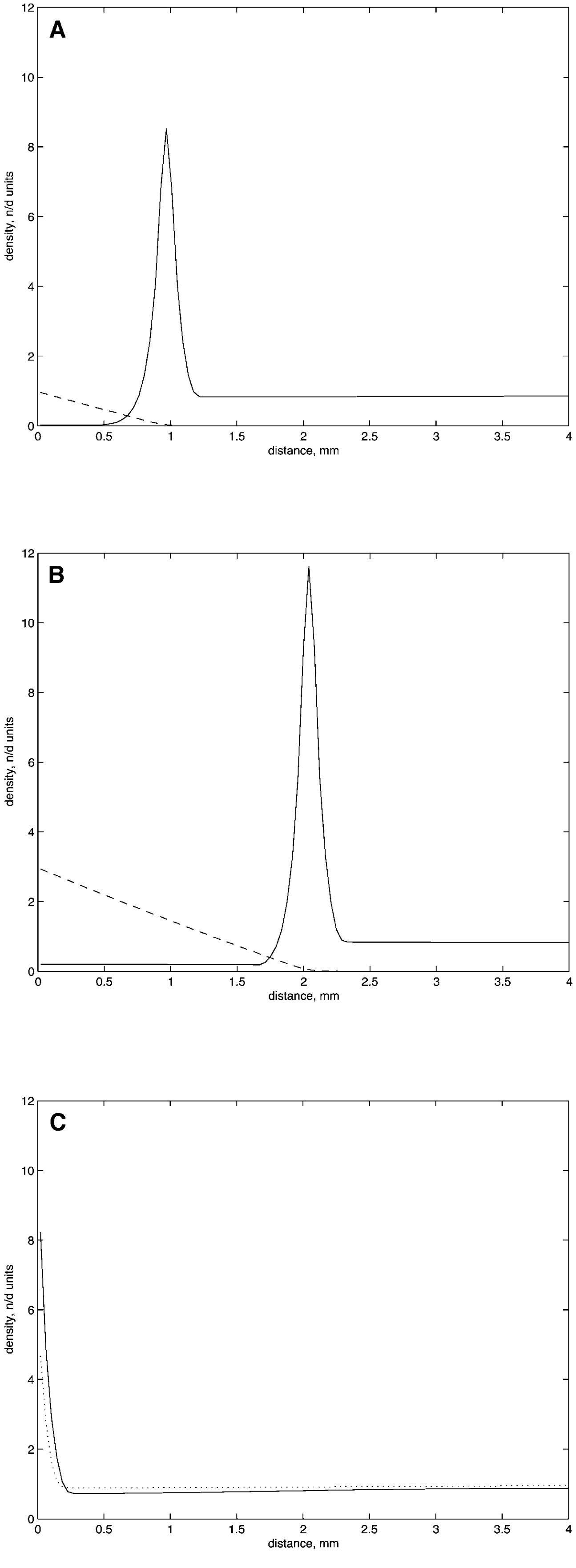

FIGURE 5 Band location, density, and width depends on the oxygen concentration at the meniscus. (*A* and *B*) Bacterial densities (*solid line*) and oxygen concentration (*dashed line*) at $L_0 = 10\%$ (*A*) and at $L_0 = 30\%$ (*B*) are shown. (*C*) Bacterial densities at $L_0 = 0.4\%$ (*solid line*) and at $L_0 = 0.2\%$ (*dotted line*) are shown. All results correspond to $t = 5$ min, initial constant bacterial density and zero oxygen density, $L_{\max} = 0.5\%$, $L_{\min} = 0.3\%$, $\tilde{L}_{\max} = 5\%$, $\tilde{L}_{\min} = 0.01\%$.

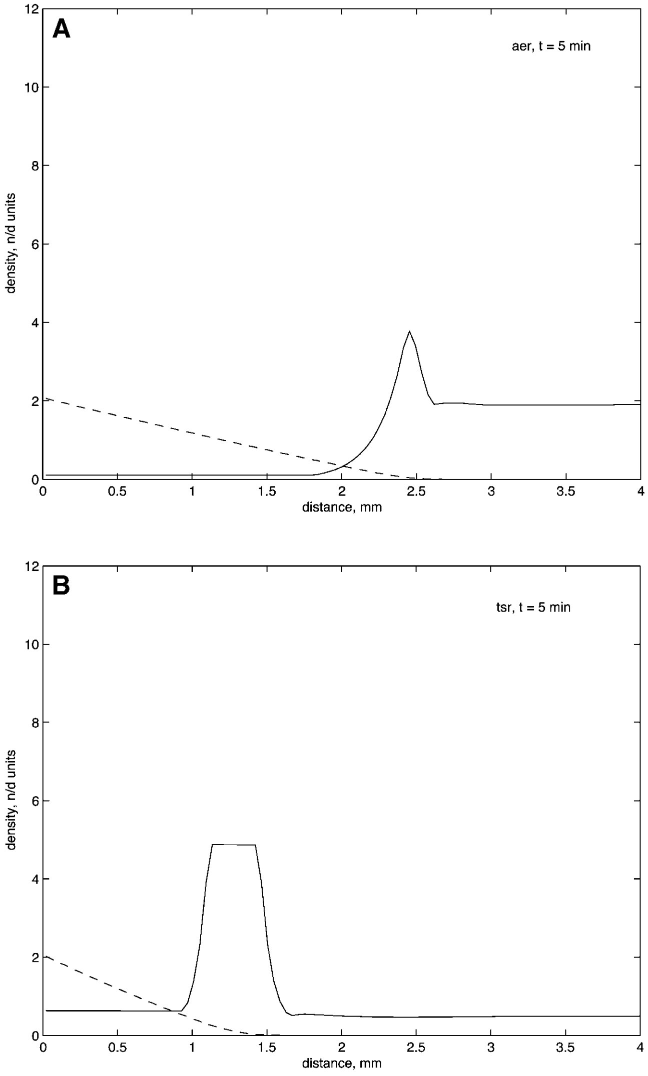

FIGURE 6 Dependence of the band location, density, and width on model parameters. The solid line shows the bacterial density developed at 5 min from the initial constant density. Dashed line shows the developed oxygen concentration. (*A*) The case corresponding to *aer* mutant: all parameters are as in Fig. 4, except $\tilde{L}_{\min} = 0.1\%$, and parameter $(F - f)$ is decreased by 70%. (*B*) The case corresponding to *tsr* mutant: all parameters are as in Fig. 4, except $L_{\max} = 2\%$, and parameter $(F - f)$ is decreased by 30%. In the simulations, the energy-sensing model of *E. coli* is coupled with the swimming behavior model of *A.b.*

inversely proportional to the square root of the initial cell density, whereas the cell density in the band is proportional to the square root of the initial cell density and to the square root of the oxygen level at the meniscus. These predictions can be tested.

Dependence of the band's location and density on model parameters

The simulations demonstrated that the location and density of the band were sensitive neither to oxygen dependent variations of the swimming speed nor to the value of the reversal frequency, F, at unfavorable oxygen concentrations (data not shown). The only minor effect of varying the speed and frequency fewfold at very low or high oxygen was a small increase of the duration of the band formation. Therefore, in the simulations we used the constant swimming speed and the reversal frequency given by Eq. 5.

We varied the values of the model parameters $L_{\min}$, $L_{\max}$, $\tilde{L}_{\min}$, $\tilde{L}_{\max}$, and $s = v/(F - f)$, which are difficult to measure accurately. The results indicate that, in general, the fewer number of cells in the band, the farther is the band from the meniscus, and vice versa. The reason is clear: a smaller number of cells consume less oxygen, so a shallower oxygen gradient is sufficient to deliver the consumed oxygen to the band. For given oxygen concentrations at the meniscus and at the band's edge, a shallower gradient corresponds to a greater distance. For example, narrowing the sensitive oxygen intervals $(\tilde{L}_{\min} < L < L_{\min})$ and $(L_{\max} < L < \tilde{L}_{\max})$ (not changing the favorable interval $(L_{\min} < L < L_{\max})$) leads to formation of a less dense band farther away from the meniscus (not shown). Decreasing the reversal frequency difference $(F - f)$ in the sensitive oxygen intervals, which means a less effective trapping of the cells in the band, has a similar effect.

We illustrate these effects in Fig. 6. Fig. 6 *A* depicts the cell density and oxygen gradient at all model parameters, except $\tilde{L}_{\min}$ and $(F - f)$, being the same as in the case illustrated in Fig. 4. The parameter $\tilde{L}_{\min}$ was increased from 0.01% to 0.1%, which decreased the lower sensitive oxygen interval, and the parameter $(F - f)$ was decreased by 70%. The resulting band was farther and less dense, and the oxygen gradient shallower, than those in Fig. 4 *D*. Fig. 6 *B* demonstrates the effect of increasing the favorable oxygen region: in this case, the parameter $L_{\max}$ was increased from 0.5% to 2%, and the parameter $(F - f)$ was decreased by 30%. Despite the slight decrease in the trapping efficiency due to the $(F - f)$ decrease, the widening of the favorable oxygen region increases the band's width, which effectively causes growth of the total number of the cells trapped in the band. All these cells consume more oxygen, so the band moves closer to the meniscus, steepening the oxygen gradient. The relevance of these cases to oxygen sensing by *aer* and *tsr* mutants is discussed below.

How the cell senses oxygen gradients

We first tested the energy-sensing model (Section ''Model of energy sensing'') by simulating Eqs. 7–11 of Appendix 1 with the initial conditions corresponding to steady-state concentrations of Tsr, Aer, Tsr*, Aer*, and CheY$_p$. First, we applied step-like shifts in time to the activation rates for Aer and Tsr, α_1 and α_2, respectively, simulating the temporal chemotactic assay. We considered three cases: i), $\alpha_1 = \alpha_2 = \alpha$ (wild-type: Aer and Tsr are equally effective); ii), $\alpha_1 = 0$, $\alpha_2 = \alpha \neq 0$ (*aer* mutant); and iii), $\alpha_1 = \alpha \neq 0$, $\alpha_2 = 0$ (*tsr* mutant). In all cases, rapid changes in CheY$_p$ concentration were followed by slower adaptation (not shown). Such characteristic temporal response usually underlies temporal comparison mechanism and taxis (Bray, 2001). In cases i and iii, CheY$_p$ concentration adapted to levels different from the initial concentration, because the signaling Aer does not adapt perfectly, in agreement with results of Almogy et al. (2001) for the secondary adaptation pathways. In case ii, the CheY$_p$ concentration adapted exactly to the baseline due to the primary perfect adaptation pathway, in agreement with results of Almogy et al. (2001) and Barkai and Leibler (1997). Note that according to Berg and Brown (1972), chemotactic signal transduced by Tar adapts exactly, but that transduced by Tsr does not, which may be of relevance to our results.

Next, to test the oxygen gradient sensing model in the spatial assay (remembering that the gradient sensing model is for *E. coli*, whereas the spatial model is for *A.b.*), we simulated model (Eqs. 7–11) of Appendix 1 in the three cases described above using the rate of activation $\alpha = 10 \pm arctan(0.1(x - x_s))$, where x_s is the middle of the sensitive region (Fig. 7). The rationale behind choosing this form of the activation rate is that the plus sign in the formula for $\alpha(t)$ corresponds qualitatively to the activation rate in a cell swimming from the left to the right in a stationary oxygen gradient changing from favorable oxygen at the left to unfavorable at the right. (The activation rate is high at the right, causing an increased CheY$_p$ concentration proportional to the reversal rate.) The corresponding receptor activation rate increases from left to right as shown in Fig. 7. A cell swimming in the direction shown by the dotted arrow is activated with the rate $\alpha(t) = 10 + arctan(0.1v(t - t_s))$, where t_s is the time of passing through the middle of the sensitive region. On the other hand, a cell swimming from the right to the left in the same oxygen gradient (shown by the solid arrow) would feel the temporal change of the activation rate given by $\alpha(t) = 10 - arctan(0.1v(t - t_s))$.

Simulations give the results illustrated in Fig. 7. In case ii of *aer* mutants, CheY$_p$ concentration (proportional to the reversal rate) adapts in both favorable and unfavorable regions due to the exact adaptation. However, in the transition zone in the middle, cells swimming to the right reverse more frequently due to effective comparison of more favorable oxygen at the left with their current conditions. Oppositely directed cells reverse less frequently. Qualitatively, this proves that Tsr alone can be responsible for the aerotactic behavior. In case iii of *tsr* mutants, similar behavior is observed, with the important difference being that the adapted CheY$_p$ concentrations in favorable and unfavorable regions are different due to the imperfect adaptation. Nevertheless, this imperfect adaptation is sufficient to explain the observed hysteresis of the reversal frequencies for the right- and left-moving cells, and so Aer alone also can govern the aerotactic behavior. Finally, the simulations show that the aerotaxis in the wild-type cells (case i) is more effective than in either of two mutants, because the difference in CheY$_p$ concentrations between the right- and left-moving cells is roughly the sum of those for the mutants (Fig. 7).

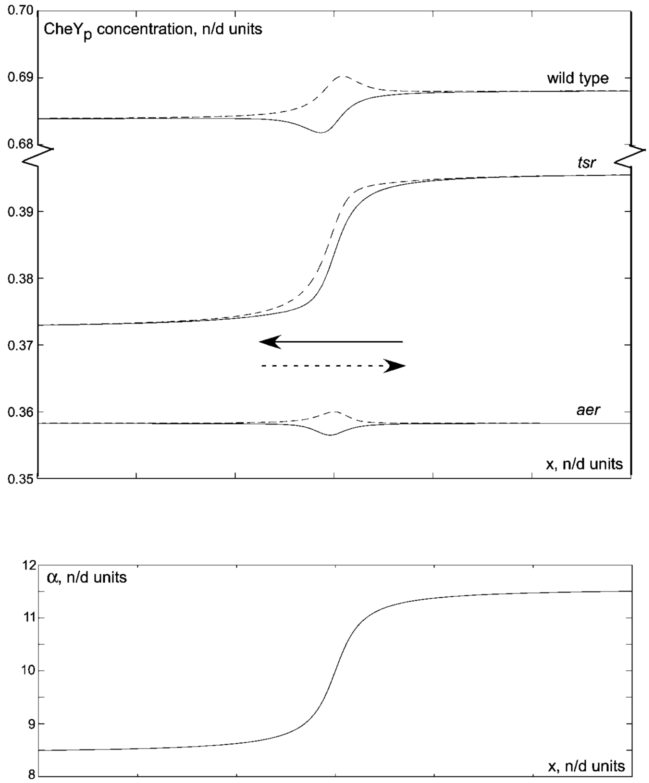

FIGURE 7 Simulations of the oxygen-sensing model in swimming *E. coli* cell. (*Bottom*) Receptor activation rate as the function of the spatial coordinate corresponds to favorable oxygen at the left and unfavorable oxygen at the right. (*Top*) Corresponding concentration of the phosphorylated CheY (proportional to the reversal frequency) as the function of the spatial coordinate in the cases of the wild-type cells and *aer* and *tsr* mutants The dashed (*solid*) curves are the reversal frequencies of the right- (left-) swimming cells.

These results provide insight into our choice of formula (Eq. 5) for oxygen dependence of the reversal frequency: graphs of the CheY$_p$ concentrations proportional to the reversal frequencies in Fig. 7 look qualitatively similar to the graphs of the reversal frequencies in Fig. 2. (We assume that CheY$_p$ concentration varies between low and intermediate values, in which case it is roughly proportional to the reversal frequency (Cluzel et al., 2000).) Also, our theoretical results are in semiquantitative agreement with observations in temporal and spatial aerotactic assays of *E. coli* (Rebbapragada et al., 1997). Similarly to the model predictions, the reversal frequency changes in either *aer* or *tsr* mutants. Also agreeing with the model, the band densities corresponding to the mutant strains were less than the density in the wild-type cells, but both mutants exhibited aerotactic behavior.

Note that Rebbapragada et al (1997) observed the band of *tsr* mutants to be less dense but closer to the meniscus than the band of wild-type cells. The band of *aer* mutants is also less dense, but it is farther from the meniscus. This phenomenon can be explained by the assumption that Aer and Tsr receptors respond differently to various oxygen concentrations. For example, the parameter $\tilde{L}_{\min}$ could be increased, and the reversal frequency differences for the right- and left-moving cells could be decreased in *aer* mutants in comparison with the wild-type cells. Fig. 6 *A* shows that in this case the band of small density and width develops farther from the meniscus. Similarly, parameter $L_{\max}$ could be increased, and the reversal frequency differences for the right- and left-moving cells could be decreased in *tsr* mutants. Fig. 6 *B* demonstrates that in this case, the band of small density, but large width, develops closer to the meniscus. These theoretical examples compare well with experimental observation (see Fig. 2 of Rebbapragada et al. (1997). Note that this figure illustrates *E. coli* behavior, whereas our simulations are based on the swimming behavior of *A.b.*).

DISCUSSION

Following Zhulin et al. (1996), we propose a model of aerotactic behavior according to which the internal cell energy is maximal in a narrow region of favorable oxygen concentration and minimal at low and high oxygen concentrations. Furthermore, the cell energy is an increasing (decreasing) function of oxygen concentration in the sensitive region between low and favorable (favorable and high) oxygen concentration. The reversal frequency is regulated by a signal transduction mechanism based on a short-term memory and is a function of both the energy level and its time derivative. This function is such that the reversal frequency is low if the cell energy is increasing or maximal and high if the cell energy is decreasing or minimal. The temporal assay for aerotaxis (Zhulin et al., 1996) provides model parameters. Computer simulations demonstrate that the parameters of the bacterial band predicted by the model agree very well with the measurements (Zhulin et al., 1996). The model also makes testable predictions about dependence of the distance between the band and the meniscus and band's cell density on the oxygen level at the meniscus and initial cell density.

We suggest a hypothetical energy-sensing model. It is based on the hypothesis that Aer and Tsr receptors share the same phospho-relay activation pathway, but use different slow adaptation pathways (a methylation-independent one for Aer and a combination of methylation-dependent and methylation-independent ones for Tsr) to respond to the changes in the cell energy level. The model simulations demonstrate that the Aer and Tsr signaling is additive (but not linearly). The model explains semiquantitatively measurements of the reversal frequency in temporal and spatial aerotactic assays. More data are needed to substantiate this idea.

One of the model's limitations is its 1-D character, which neglects deviations of the swimming trajectories from straight paths across the band. Another limitation is an unknown, presumably small, effect of the finite adaptation time, which makes the reversal frequency a function of the recent ''history'' of reversals and runs, rather than a local function of oxygen concentration and its derivatives. These limitations can be removed in a framework of 3-D Monte Carlo simulations. Such future modeling, as well as the simpler differential equation approach in this article, is a very useful research tool complementary to traditional experimental methods.

APPENDIX 1: EQUATIONS OF THE ENERGY-SENSING MODEL

We use the following equations to quantify the model introduced in Section ''Model of energy sensing'' (Fig. 3):

$$\frac{dA^*}{dt} = (\alpha_1(1 - A^*) - k_1A^*), \tag{7}$$

$$\frac{dT^*}{dt} = (\alpha_2T - k_2T^*) - bT^*, \tag{8}$$

$$\frac{dT}{dt} = (-\alpha_2T + k_2T^*) + r, \tag{9}$$

$$\frac{dY}{dt} = (k_3A^* + k_4T^*)(1 - Y) - k_5YZ, \tag{10}$$

$$\frac{dZ}{dt} = k_6Y - k_7Z. \tag{11}$$

Here A^* is the activated Aer concentration. Total Aer concentration is normalized by 1. Equation 7 describes a simple activation kinetics of Aer → Aer* with the rate α_1 and inverse rate k_1. Equations 8 and 9 quantify the reduced model (Barkai and Leibler, 1997), where the expressions in parentheses are responsible for a fast activation kinetics of methylated Tsr receptors (active and inactive methylated Tsr concentrations are T^* and T, respectively; Tsr → Tsr* with the rate α_2 and inverse rate k_2). The parameter r is the rate of CheR-mediated saturated methylation, and b is the rate of CheB-mediated demethylation (for simplicity, we use the constant demethylation rate, not the Michaelis-Menten rate of model (Barkai and Leibler, 1997)). Equations 10 and 11 describe the modified and reduced model (Almogy et al., 2001), where Y is the CheY$_p$ concentration (total concentration of CheY is normalized by 1). The variable Z denotes the activated CheZ concentration (CheZ$_a$). We neglect some pathways analyzed in Almogy et al. (2001) and simplify kinetics of CheZ activation by CheY$_p$. We assume that CheY$_p$ activates CheZ at saturation with the rate k_6, that CheZ$_a$ de-activates spontaneously with the rate k_7, and that the rate of CheY$_p$ dephosphorylation is proportional to the product of CheZ$_a$ and CheY$_p$ concentrations with the proportionality coefficient k_5. We also assume that Aer and Tsr phosphorylate CheY with the rates k_3 and k_4, respectively.

We simulated the system of Eqs. 7–11 using the following values of the parameters: $k_1 = 10$; $k_2 = 10$; $k_3 = 5$; $k_4 = 5$; $k_5 = 1$; $k_6 = 1$; $k_7 = 0.5$; $r = 1$; $b = 0.4$; and $\alpha_{1,2} \sim 10$. Our model is semiquantitative, and we justify this choices by taking some of the parameter values similar to those in Almogy et al. (2001), adjusting parameters of the perfect adaptation submodel so that the models of Almogy et al. (2001) and Barkai and Leibler (1997) describe signals of similar durations and amplitudes, and ensuring proper timescale separations between fast and slow processes. The results of the simulations are described in Section ''How the cell senses oxygen gradients''.

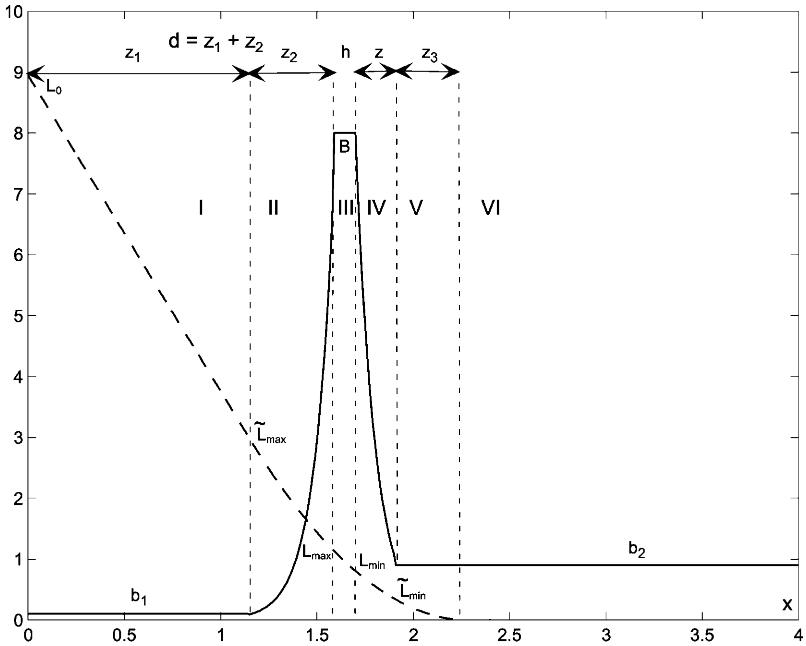

FIGURE 8 Steady-state distributions of oxygen (*dashed lines*) and bacteria (*solid lines*) found analytically in different regions (*I–VI*) across the capillary. The notations for the densities, concentrations, and distances are explained in the text.

APPENDIX 2: SCALING AND NUMERICAL ANALYSIS

Relevant length scales in the aerotactic spatial assay are the length of the capillary, S, and the width of the bacterial band. The order of magnitude of S is millimeters. (All parameters are listed in Table 2.) Below, we demonstrate that the order of magnitude of the band's width is equal to the swimming speed divided by the reversal frequency difference, $s = \nu/(F - f) = 100\ \mu\text{m}$.

Six relevant time scales (T_i, $i = 1 - 6$) characterize the spatial assay for aerotaxis:

If the oxygen diffuses freely into the capillary, than at time t its density profile is given by the formula $L(x,t) = L_0(1 - er\ \ f(x/\sqrt{4Dt}))$ (Berg, 1983), and by the depth of oxygen penetration into the capillary $x \sim 2\sqrt{Dt}$. The oxygen penetrates to a ~1 mm depth in $T_1 \sim (1\ \text{mm})^2/2D \sim 4$ min.

The time for a bacterium swimming without reversals to escape high oxygen concentrations near the meniscus and to reach the favorable oxygen concentration at a ~1 mm depth is $T_2 \sim (1\ \text{mm})/\nu \sim 1$ min.

The time over which the cells in the dense band (cell density $\sim 10b_0$) consume the oxygen dissolved in water is $T_3 \sim L_0/(\kappa \cdot 10b_0) \sim 3$ min.

Effective diffusion coefficient for the bacteria behind the band executing a random walk is $D_b \sim \nu^2/F \sim 3 \cdot 10^3\ \mu\text{m}^2/\text{s}$. Characteristic time for the cell density behind the band to relax to the constant equilibrium distribution is $T_4 \sim (1\ \text{mm})^2/D_b \sim 5$ min.

The four timescales above indicate that the characteristic development time for the band is of the order of a few minutes. To simulate the fine details of the band's development, we must take into account relevant "fast" timescales defined by the following arguments. In the first few seconds, oxygen penetrates the capillary faster ($x \sim \sqrt{t}$) than the cells escaping high oxygen concentrations (x t), but later the cells outrun the oxygen diffusion. The crossover takes place when $2\sqrt{Dt} \sim \nu t$, or at $T_5 \sim 4D/\nu^2 \sim 5$ s. Also, swimming across the band takes $T_6 \sim s/\nu \sim 2.5$ s.

To nondimensionalize the model equations, we use the value $s = 100\ \mu\text{m}$ as the length scale and choose it as the discretization spatial step for the numerical analysis to be able to reproduce the details of the spatial pattern. Thus, we discretize the spatial domain into 4 mm/0.1 mm = 40 intervals. Smaller spatial steps would give finer resolution, but would require much longer computation time. To nondimensionalize the model equations, we used $T_6 = 2.5$ s as the timescale, and L_0 and b_0 as the scales for the oxygen concentration and bacterial density, respectively.

The equations for left- (right-) moving bacteria were solved with a forward- (backward-) difference scheme (Garcia, 1994). The reaction-diffusion equation for the oxygen was integrated using a forward-time, centered space scheme (Garcia, 1994). The size of the time step (0.001 time unit) was sufficiently small for stability. The simulations were run for 200 time units (~8 min of real time).

APPENDIX 3: ANALYSIS OF THE STEADY-STATE DISTRIBUTIONS

The numerical analysis of the model shows that in a few minutes, the bacterial and oxygen distributions asymptotically converge to the stable steady state. These steady-state distributions can be analyzed because of the piecewise linear character of the model equations. From here on, we refer explicitly to the stationary solutions of the model equations. It is easy to show that the oxygen concentration, $L(x)$, is a nonincreasing function of x on the interval [0, S]. Therefore, the interval [0, S] can be divided into six subintervals separated by the five points in which the oxygen concentration is equal to five special oxygen levels (Fig. 8), namely:

Region I: $0 < x < z_1$, $L(0) = L_0$, $L(z_1) = \tilde{L}_{\max}$;
Region II: $z_1 < x < d = z_1 + z_2$, $L(d) = L_{\max}$;
Region III: $d < x < d + h$, $L(d + h) = L_{\min}$;
Region IV: $d + h < x < d + h + z$, $L(d + h + z) = \tilde{L}_{\min}$;
Region V: $d + h + z < x < d + h + z + z_3$, $L(d + h + z + z_3) = 0$;
Region VI: $d + h + z + z_3 < x < S$, $L(x) = 0$.

In the steady state, the flux of bacteria is zero everywhere, so $r(x) = l(x)$, and we use the cell density $b(x) = r(x) + l(x) = 2r(x)$ as the model variable.

We will also use the notations $k = \kappa/D$, $s = v/(F - f)$ and prime sign for spatial derivatives. The steady-state solutions of the model equations can be found region by region as follows:

Region I: The bacterial density is given by: $-\nu r' - Fr + Fl = 0$, $\nu l' + Fr - Fl = 0$. By adding the two equations and using the equality $r = l$, we obtain: $b = b_1 =$ const. The equation for oxygen in this region is: $L'' = kb = kb_1$, which has the solution: $L(x) = L_0 - c_0 x + kb_1/2x^2$.

Region II: The bacterial density is given by: $-\nu r' - fr + Fl = 0$, $\nu l' + fr - Fl = 0$. By subtracting the two equations and using the equality $r = l$, we obtain: $b = b_1 e^{(x - z_1)/s}$. The equation for oxygen in this region is: $L'' = kb = kb_1 e^{(x - z_1)/s}$, which has the solution: $L(x) = \tilde{L}_{max} - c_1(x - z_1) + kb_1 s^2 [e(^{x - z_1)/s} - 1]$.

Region III: The bacterial density is given by: $-\nu r' - fr + fl = 0$, $\nu l' + fr - fl = 0$. By adding the two equations and using the equality $r = l$, we obtain: $b = B =$ const. The equation for oxygen in this region is: $L'' = kB$, which has the solution: $L(x) = L_{\max} - c_2(x - d) + kB/2(x - d)^2$.

Region IV: The bacterial density is given by: $-\nu r' - Fr + fl = 0$, $\nu l' + Fr - fl = 0$. By subtracting the two equations and using the equality $r = l$, we obtain: $b = Be^{-(x - d - h)/s}$. The equation for oxygen in this region is: $L'' = kb = kBe^{(x - d - h)/s}$, which has the solution: $L(x) = \tilde{L}_{\min} - c_3(x - d - h) + kBs^2[e^{(x - d - h)/s} - 1]$.

Region V: The bacterial density is given by: $-\nu r' - Fr + Fl = 0$, $\nu l' + Fr - Fl = 0$. By adding the two equations and using the equality $r = l$, we obtain: $b = b_2 =$ const. The equation for oxygen in this region is: $L'' = kb_2$, which has the solution: $L(x) = \tilde{L}_{min} - c_4(x - d - h - z) + kb_2/2(x - d - h - z)^2$.

Region VI: The bacterial density is the same as in Region V, and $L(x) = 0$.

The expressions for the distributions of oxygen and bacteria in the six regions depend on 13 unknown parameters: c_0, c_1, c_2, c_3, c_4, z, z_1, z_2, z_3, h, b_1, b_2, and B. These parameters can be found from the 13 boundary conditions at the edges of the regions:

Five conditions for continuity of the oxygen concentration at the five boundaries between the six regions. For example, $L_{\text{I}}(z_1) = L_{\text{II}}(z_1)$, where $L_{\text{I}}(x)$ and $L_{\text{II}}(x)$ are the oxygen concentrations in Regions I and II, respectively.

Five conditions for continuity of the oxygen flux at the five boundaries between the six regions, which means continuity of the first spatial derivatives of the oxygen concentration. For example, $L'_{\text{I}}(z_1) = L'_{\text{II}}(z_1)$.

Two conditions for continuity of the bacterial density at the boundaries between Regions II and III ($b_1 e^{z_2/s} = B$) and between Regions IV and V ($Be^{-z/s} = b_2$). (Continuity at the other boundary is already taken care of by the form of the analytical expressions for the density written above.)

Condition for the conservation of the total number of bacteria:

$$b_0 S = b_1 z_1 + B(h + s[2 - e^{-z/s} - e^{-z_2/s}]) + b_2(S - z - h - z_1 - z_2 - z_3).$$

These 13 conditions provide 13 highly nonlinear algebraic equations. The number and nonlinearity of these equations make it very hard to prove rigorously that they have a unique solution. Empirical numerical experiments, though, indicate that the solution to these equations exists and that it is unique. The numerical estimates show that at $L_0 = 21\%$, $b_1 \approx 0$, $b_2 \approx b_0$, $B \approx 8b_0$, $d \approx 1.6$ mm, $z, z_2 \sim s$, and $h \ll s$. The corresponding analytically found bacterial and oxygen distribution plotted in Fig. 8 (the scale of the oxygen distribution is distorted to blow up the regions of low oxygen concentrations) agree well with both numerical solution and experimental observations. One of the important results of this analysis is that the band's width, which can be defined as $w = 2s + h$ is approximately equal to $2s \approx 200$ μm.

Further approximate analysis provides more insight into the dependence of the band's dimensions on the model parameters. First, using the insensitivity of the steady-state distributions to $\tilde{L}_{\max}$, we approximate $\tilde{L}_{\max} \approx L_0$, which makes $z_1 = 0$. Also, we use the approximate equality $b_2 \approx b_0$. Finally, the equation for b_1 and equations for the distributions in the Regions V and VI are uncoupled from the other equations. These simplifications and approximations leave us with seven unknown parameters ($d = z_2$, h, z, B, c_1, c_2, and c_3) and seven boundary conditions:

1. Continuity of the bacterial density at the boundary between Regions IV and V: $Be^{-z/s} = b_0$;
2. Conservation of the total number of bacteria: $b_0(d + h + z) = B(h + s[2 - e^{-z/s} - e^{-d/s}])$;
3. Continuity of oxygen at the boundary between Regions II and III: $L_0 - c_1 d + kBs^2[1 - e^{-d/s}] = L_{\max}$;
4. Continuity of oxygen at the boundary between Regions III and IV: $L_{\max} - c_2 h + 1/2\, kBh^2 = L_{\min}$;
5. Continuity of oxygen at the boundary between Regions IV and V: $L_{\min} - c_3 z - kBs^2[e^{-z/s} - 1] = \tilde{L}_{\min}$;
6. Continuity of the flux of oxygen at the boundary between Regions II and III: $-c_1 + kBs = -c_2$;
7. Continuity of the flux of oxygen at the boundary between Regions III and IV: $-c_2 + kBh = -c_3 - kBs$.

Let us introduce the notations $\lambda = e^{z/s}$, $\varepsilon_1 = L_{\max}/L_0$, $\varepsilon_2 = L_{\min}/L_0$, $\varepsilon_3 = \tilde{L}_{\min}/L_0$ and rescale the boundary conditions using b_0 as the unit of the bacterial density, L_0 as the unit of the oxygen concentration, and s as the unit of length. Then, the first condition is simply $B = \lambda$, and the other six boundary conditions have the form:

$$\lambda(h + 2 - e^{-d} - \lambda^{-1}) = d + h + z, \tag{12}$$

$$c_1 d - k\lambda(1 - e^{-d}) = 1 - \varepsilon_1, \tag{13}$$

$$c_2 h - k\lambda h^2/2 = \varepsilon_1 - \varepsilon_2, \tag{14}$$

$$c_3(ln(\lambda)) + k(\lambda - 1) = \varepsilon_2 - \varepsilon_3, \tag{15}$$

$$-c_1 + k\lambda = -c_2, \tag{16}$$

$$-c_2 + k\lambda h = -c_3 - k\lambda. \tag{17}$$

Some analysis demonstrates that λ, $d \gg 1$, $h \ll 1$ as far as $\varepsilon_{1,2,3} \ll 1$ (which is the case when $L_0 \gg 1\%$). Then, from Eq. 12, we have $d \approx 2\lambda$, and Eq. 14 can be uncoupled from the rest of the system. The other four equations can be written in the form:

$$(2c_1 - k)\lambda \approx 1, \quad c_3(ln(\lambda)) + k\lambda \approx 0,$$
$$-c_1 + k\lambda = -c_2, \quad -c_2 \approx -c_3 - k\lambda.$$

Expressing c_1 and c_3 in terms of c_2 from the last two equations, substituting the resulting expression into the first two equations, and eliminating c_2 from the resulting two equations, we have the algebraic equation for λ:

$$k\lambda[2\lambda(ln(\lambda)) - ln(\lambda) - \lambda] \approx ln(\lambda).$$

At $\lambda \gg 1$, $2\lambda(ln(\lambda)) \gg \lambda$, $ln(\lambda)$, so we finally find the following rough approximation: $2\lambda \approx 1/\sqrt{k}$. Knowing λ, it is easy to estimate d, B, z, and h. The dimensional expressions for these parameters characterizing the band are:

$$d \approx \sqrt{\frac{DL_0}{\kappa b_0}}, \quad z \approx 2.5s, \quad h \approx 0.3s, \quad B \approx \sqrt{\frac{DL_0 b_0}{4\kappa s^2}}. \tag{18}$$

The biological implications of this result are discussed in "Results".

Similar analysis is possible in the case when the oxygen level at the meniscus drops to the level of $L_{\max}$ or $L_{\min}$. Corresponding algebraic equations can be solved only numerically. These solutions demonstrate that the band appears right at the air-water interface, that the density of the bacteria in the band is a fewfold greater than b_0, and that the width of the band is $\sim s$. Furthermore, the density and width of the band in these cases are decreasing functions of L_0, which supports both numerical results and experimental observations.

We are grateful to H. Berg, D. Bray, L. Edelstein-Keshet, S. Aksenov, and K. Larripa for fruitful discussions and to anonymous reviewers for helpful suggestions.

A.M. and B.M. were supported by the University of California, Davis, Chancellor's Fellowship; National Science Foundation grant DMS-0073828; and National Institutes of Health Glue Grant ''Cell Migration Consortium''. I.Z. was supported by National Science Foundation grant EIA-0219079.

REFERENCES

Adler, J. 1988. Chemotaxis: old and new. *Bot. Acta.* 101:93–100.

Alexandre, G., R. Bally, B. L. Taylor, and I. B. Zhulin. 1999. Loss of cytochrome c oxidase activity and acquisition of resistance to quinone analogs in a laccase-positive variant of *azospirillum lipoferum*. *J. Bacteriol.* 181:6730–6738.

Alexandre, G., and I. B. Zhulin. 2001. More than one way to sense chemicals. *J. Bacteriol.* 183:4681–4686.

Almogy, G., L. Stone, and N. Ben-Tal. 2001. Multi-stage regulation, a key to reliable adaptive biochemical pathways. *Biophys. J.* 81:3016–3028.

Barak, R., I. Nur, Y. Okon, and Y. Henis. 1982. Aerotactic response of *Azospirillum brasilense*. *J. Bacteriol.* 152:643–649.

Barkai, N., and S. Leibler. 1997. Robustness in simple biochemical networks. *Nature.* 387:913–917.

Berg, H. C. 1983. Random Walks in Biology. Princeton University Press, Princeton, NJ.

Berg, H. C., and D. A. Brown. 1972. Chemotaxis in *Escherichia coli* analyzed by three-dimensional tracking. *Nature.* 239:500–504.

Bibikov, S. I., R. Biran, K. E. Rudd, and J. S. Parkinson. 1997. A signal transducer for aerotaxis in *Escherichia coli*. *J. Bacteriol.* 179:4075–4079.

Bourret, R. B., and A. M. Stock. 2002. Molecular information processing: lessons from bacterial chemotaxis. *J. Biol. Chem.* 277:9625–9628.

Bray, D. 2001. Cell Movements. Garland Publishing, New York.

Bray, D., R. B. Bourret, and M. I. Simon. 1993. Computer simulation of the phosphorylation cascade controlling bacterial chemotaxis. *Mol. Biol. Cell.* 4:469–482.

Brown, D. A., and H. C. Berg. 1974. Temporal simulation of chemotaxis in *Escherichia coli*. *Proc. Natl. Acad. Sci. USA.* 71:1388–1392.

Cluzel, P., M. Surette, and S. Leibler. 2000. An ultrasensitive bacterial motor revealed by monitoring signaling proteins in single cells. *Science.* 287:1652–1655.

Dang, C. V., M. Niwano, J. Ryu, and B. L. Taylor. 1986. Inversion of aerotactic response in *Escherichia coli* deficient in CheB protein methylesterase. *J. Bacteriol.* 166:275–280.

Engelmann, T. W. 1881. Neue methode zur untersuchung der sauerstoffausscheidung pflanzlicher und tierischer organismen (New method for investigation of oxygen-searching plant and animal organisms). *Pflugers Arch. Gesammte Physiol.* 25:285–292.

Feng, X., J. W. Baumgartner, and G. L. Hazelbauer. 1997. High- and low-abundance chemoreceptors in *Escherichia coli*: differential activities associated with closely related cytoplasmic domains. *J. Bacteriol.* 179:6714–6720.

Garcia, A. I. 1994. Numerical Methods for Physicists. Prentice Hall, Englewood Cliffs, NJ.

Glagolev, A. N. 1980. Reception of the energy level in bacterial taxis. *J. Theor. Biol.* 82:171–185.

Hillesdon, A. J., and T. J. Pedley. 1996. Bioconvection in suspensions of oxytactic bacteria: linear theory. *J. Fluid Mech.* 324:223–259.

Hillesdon, A. J., T. J. Pedley, and J. O. Kessler. 1995. The development of concentration gradients in a suspension of chemotactic bacteria. *Bull. Math. Biol.* 57:299–344.

Hou, S., R. W. Larsen, D. Boudko, C. W. Riley, E. Karatan, M. Zimmer, G. W. Ordal, and M. Alam. 2000. Myoglobin-like aerotaxis transducers in archaea and bacteria. *Nature.* 403:540–544.

Jennings, M. S., and J. H. Crosby. 1901. Studies on reactions to stimuli in unicellular organisms: the manner in which bacteria react to stimuli, especially to chemical stimuli. *Am. J. Physiol.* 6:31–37.

Keller, E., and L. Segel. 1971. Model for chemotaxis. *J. Theor. Biol.* 30:225–234.

Li, J., G. Li, and R. M. Weis. 1997. The serine chemoreceptor from *Escherichia coli* is methylated through an inter-dimer process. *Biochemistry.* 36:11851–11857.

Mello, B. A., and Y. Tu. 2003. Perfect and near-perfect adaptation in a model of bacterial chemotaxis. *Biophys. J.* 84:2943–2956.

Niwano, M., and B. L. Taylor. 1982. Novel sensory adaptation mechanism in bacterial chemotaxis to oxygen and phosphotransferase substrates. *Proc. Natl. Acad. Sci. USA.* 79:1115–1126.

Nossal, R. 1976. Directed cell motion arising from strongly biased turn angles. *Math. Biosci.* 31:121–129.

Othmer, H. G., and T. Hillen. 2002. Chemotaxis equations from the diffusion limit of transport equations. *SIAM J. Appl. Math.* 62:1222–1250.

Othmer, H. G., and P. Schaap. 1998. Oscillatory camp signaling in the development of *Dictyostelium discoideum*. *Comm. Theor. Biol.* 5:175–282.

Rebbapragada, A., M. S. Johnsona, G. P. Harding, A. J. Zuccarelli, H. M. Fletcher, I. B. Zhulin, and B. L. Taylor. 1997. The Aer protein and serine chemoreceptor Tsr independently sense intracellular energy levels and transduce oxygen, redox, and energy signals for *Escherichia coli* behavior. *Proc. Natl. Acad. Sci. USA.* 94:10541–10546.

Repik, A., A. Rebbapragada, M. S. Johnson, J. O. Haznedar, I. B. Zhulin, and B. L. Taylor. 2000. Pas domain residues involved in signal transduction by the Aer redox sensor of *Escherichia coli*. *Mol. Microbiol.* 36:806–816.

Rivero, M. A., R. T. Tranquillo, H. M. Buettner, and D. A. Lauffenburger. 1989. Transport model for chemotactic cell populations based on individual cell behavior. *Chem. Eng. Sci.* 44:2881–2897.

Rowsell, E. H., J. M. Smith, A. Wolfe, and B. L. Taylor. 1995. CheA, CheW, and CheY are required for chemotaxis to oxygen and sugars of the phosphotransferase system in *Escherichia coli*. *J. Bacteriol.* 177:6011–6014.

Schnitzer, M. J., S. M. Block, H. C. Berg, and E. M. Purcell. 1990. Strategies for chemotaxis. *Symp. Soc. Gen. Microbiol.* 46:15–34.

Segel, L. A., A. Goldbeter, P. N. Devreotes, and B. E. Knox. 1986. A mechanism for exact sensory adaptation based on receptor modification. *J. Theor. Biol.* 120:151–179.

Shioi, J., R. C. Tribhuwan, S. T. Berg, and B. L. Taylor. 1988. Signal transduction in chemotaxis to oxygen in *Escherichia coli* and *Salmonella typhimurium*. *J. Bacteriol.* 170:5507–5511.

Spiro, P. A., J. S. Parkinson, and H. G. Othmer. 1997. A model of excitation and adaptation in bacterial chemotaxis. *Proc. Natl. Acad. Sci. USA.* 94:7263–7268.

Taylor, B. L. 1983. Role of proton motive force in sensory transduction in bacteria. *Annu. Rev. Microbiol.* 37:551–573.

Taylor, B. L., and M. S. Johnson. 1998. Rewiring a receptor: negative output from positive input. *FEBS Lett.* 425:377–381.

Taylor, B. L., and I. B. Zhulin. 1998. In search of higher energy: metabolism-dependent behaviour in bacteria. *Mol. Microbiol.* 28:683–690.

Taylor, B. L., and I. B. Zhulin. 1999. Pas domains: internal sensors of oxygen, redox potential, and light. *Microbiol. Mol. Biol. Rev.* 63:479–506.

Taylor, B. L., I. B. Zhulin, and M. S. Johnson. 1999. Aerotaxis and other energy-sensing behavior in bacteria. *Annu. Rev. Microbiol.* 53:103–128.

Wong, L. S., M. S. Johnson, I. B. Zhulin, and B. L. Taylor. 1995. Role of methylation in aerotaxis in *Bacillus subtilis*. *J. Bacteriol.* 177:3985–3991.

Zhulin, I. B., and J. P. Armitage. 1993. Motility, chemokinesis, and methylation-independent chemotaxis in *Azospirillum brasilense*. *J. Bacteriol.* 175:952–958.

Zhulin, I. B., V. A. Bespalov, M. S. Johnson, and B. L. Taylor. 1996. Oxygen taxis and proton motive force in *Azospirillum brasilense*. *J. Bacteriol.* 178:5199–5204.